Journal of Power Sources 448 (2020) 227468

Contents lists available at ScienceDirect

Journal of Power Sources

journal homepage: www.elsevier.com/locate/jpowsour

Deformation and failure behaviors of anode in lithium-ion batteries: Model and mechanism

Lubing Wang [a,b], Xudong Duan [a,b], Binghe Liu [a,b], Q.M. Li [c], Sha Yin [a,b], Jun Xu [a,b,*]

[a] Vehicle Energy & Safety Laboratory (VESL), Beihang University, Beijing, 100191, China
[b] Department of Automotive Engineering, School of Transportation Science and Engineering, Beihang University, Beijing, 100191, China
[c] School of Mechanical, Aerospace and Civil Engineering, The University of Manchester, Manchester, M13 9PL, UK

HIGHLIGHTS

- A multiscale detailed computational model describing anode behavior is established.
- Strain-rate dependent failure of the active material is responsible for the anode behavior.
- The binder contents and its mechanical properties effect is discussed.
- Interfacial strength between active layer and copper foil is studied.

GRAPHICAL ABSTRACT

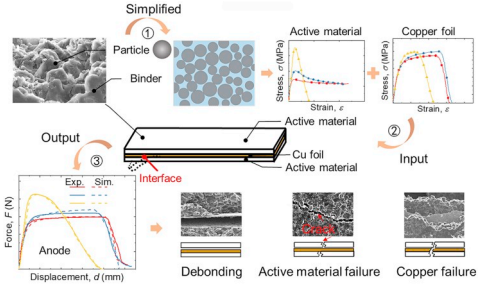

ARTICLE INFO

Keywords:
Lithium-ion battery
Anode material
Strain-rate dependent behavior
Safety
Computational modeling

ABSTRACT

Deformation and failure behaviors of the anode material play important roles in internal short-circuit and thermal runaway behaviors of lithium-ion batteries. In previous research, we discovered that anode behaves significantly different in constitutive behaviors at various strain rates. To unravel the fundamental mechanism, a multiscale detailed computational model describing anode behavior is established in the present study. Numerical simulation results of anode material show that the established model has a good correlation with the experiments for the description of the mechanical behaviors of the anode at strain-rates from 5×10^{-4}/s to 1×10^{-1}/s. This model shows that the high strain-rate dependency of the failure of the active material should be responsible for the observed deformation behavior of the anode material. Meanwhile, it is found that the particle size distribution and mechanical properties of the binder have an influential effect on the yield strength value of the anode. Results clarify the fundamental reasons for the behaviors of anode material, which may support the design of safer and more robust batteries.

1. Introduction

The safety issues of lithium-ion batteries have attracted increasing public attentions due to their wider applications in electric vehicles [1,2], cell phones [3,4], power tools [1,5] and laptops [6]. Serving as a power source, normal and abusive working scenarios of the Lithium-ion battery may both cause significant deformation of anode material [7–9]. Inevitable external mechanical abuse, internal defects and cycling of the Lithium-ion battery will cause the electrochemical reactions coupled with mechanical degradation (the mechanical fracture of the material

* Corresponding author. Vehicle Energy & Safety Laboratory (VESL), Beihang University, Beijing, 100191, China.
E-mail address: junxu@buaa.edu.cn (J. Xu).

https://doi.org/10.1016/j.jpowsour.2019.227468
Received 5 July 2019; Received in revised form 29 October 2019; Accepted 14 November 2019
Available online 21 November 2019
0378-7753/© 2019 Elsevier B.V. All rights reserved.

and structural failure of the electrode) in anode. Then, it will deteriorate the performance of lithium-ion batteries, and may subsequently lead to internal short circuit of the deteriorated battery, causing fire or explosion [10–13]. Liu et al. [14] has reviewed the safety issues and mechanisms of Lithium-ion battery cell upon mechanical abusive loading. Particularly, in dynamic mechanical abusive loading scenarios, e.g. crash, impact and drop, batteries usually have a much quick short circuit phenomenon than in quasi-static loading condition [15,16]. Therefore, a full understanding of the mechanical behaviors of anode with strain-rate dependency is in pressing need for a better battery safety design.

Anode is a kind of three-layer composite material where the inner layer is the current collector made by copper foil [17], and the outer layer is an active material mixed by binder and active particles [18,19]. To understand the overall behaviors of the anode, each component material should be fully characterized. Some mechanical behavior investigations [20–22], microscopic observations [23,24] and theoretical derivation [24,25] of components were reported in available literature. The copper foil used for Lithium-ion batteries is usually made by rolling process or electrolysis [26]. There is little research on the strain rate effect of copper foil prepared by these methods. For laser shocked polycrystalline copper, dislocation slip, profuse twins and stacking faults (SFs) coexist in copper foil where profuse twins and SFs are more dependent on strain-rate (at high strain rate) which may be used to explain the strength hardening and early failure of the copper foil [20]. Besides, the deformation twinning can also be observed at low strain rate ($\sim 10^{-2}\ s^{-1}$) [27]. As for active material, binder plays an important role in mechanical integrity of the anodes for lithium-ion batteries. Pioneering work produced by Chen et al. [22] investigated the roles of binders in the mechanical integrity of electrodes for lithium-ion batteries by coupled microscratch and digital image correlation (DIC) techniques. It was discovered that particle-particle cohesion strength increases while the interface adhesion strength between foil and particle decreases with increasing binder contents (defined as volume ratio between binder and active materials). Yim et al. [28] systematically studied the mechanical characterization of various binder materials to estimate the suitability of various binder materials and proved that fine tuning of the binder properties through an understanding of individual binders could be an efficient approach to prevent deterioration of anode.

In the meantime, we previously discovered that the stress-strain behavior of the anode changes abruptly once the strain-rate reaches 0.1/s with much higher failure stress and smaller failure strain [29], unlike the traditional strain-rate dependent behavior where the yield stress increases by strain-rate while keeping the similar profiles [30,31]. Which component materials have the essential factor to make such interesting behavior is still unknown. Therefore, insightful investigation on the fundamental mechanism of such deformation and failure behavior is worthwhile to bridge the gap for the understanding of battery safety.

This paper is organized as follows. In Section 2, modeling methodologies of active material and anode material are introduced respectively. Typical results are fully presented in Section 3. Besides, the particle size distribution effect, mechanical behavior of binder, interfacial strength effect as well as thickness effect are thoroughly discussed in Section 4.

2. Method

2.1. Analytical calculation

Anode is a layered structure material with the copper foil sandwiched by two layers of active material (Fig. 1a). Although the mechanical behaviors of the anode material, as well as the copper foil have been thoroughly characterized [29], the mechanical properties of the active materials still remain unknown since the active layer is difficult to peel off completely from the anode, and the characterization technique requires high accuracy nano-indentation method which is difficult to achieve. Therefore, we indirectly calculate its modulus and yield stress through the following analysis.

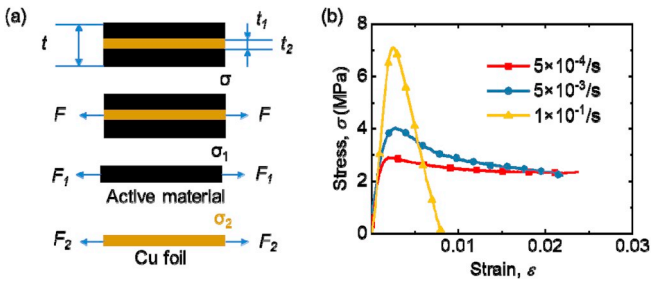

Fig. 1. (a) Schematic diagram of the composite structure anode and its force analysis; (b) Stress-strain curve of active material at strain-rates of 5×10^{-4}/s, 5×10^{-3}/s and 1×10^{-1}/s obtained from analytical calculation.

The deformation of the anode keeps uniformly before material failure under tensile test (with concentrated loading F), indicating that the copper foil and the active material share the same deformation (strain ε) before failure (interface/material failure), i.e. $\varepsilon = \varepsilon_1 = \varepsilon_2$. The total force of the anode F is shared by two layers of active particles F_1 and a single layer of copper foil F_2, i.e. $F = 2F_1 + F_2$. The thickness of the anode $t = 2t_1 + t_2$, where t_1 is the thickness of a single layer of active material, and t_2 is the thickness of copper foil. The stress-strain curves of anode material and copper foil were studied experimentally in a previous study [29] and both of them show the obvious strain-rate dependency. Therefore, based on the stress formula $F = \sigma A$ and Hooke's law, we can finally get the stress-strain relationship of the active material, $\sigma_1 = \frac{\sigma t - \sigma_2 t_2}{2t_1}$, as shown in Fig. 1b. The modulus and the yield stress of active material under different strain-rates can then be calculated, i.e. modulus is 2000 MPa, the yield stress at strain-rate 5×10^{-4}/s, 5×10^{-3}/s, and 1×10^{-1}/s are 2.7 MPa, 3.4 MPa, and 6.8 MPa, respectively.

2.2. Active material modeling

Active material is a mixture of binder and active particle, where the binder is a kind of polymeric material made by carboxymethylcellulose (CMC) [32] and the particle is stiff solid material usually made by graphite. The air voids always exist within the mixture of binder and particles, forming the pore between binder and particles with the general porosity 30% [33]. The volume fraction of the binder and particle are 9% and 61%, which can be calculated from Ref. [34] before calendered. Besides, it has been shown that stresses and plastic strains of the active material predicted by 3D models are close to those predicted using simpler 2D models of the microstructure [35]. Based on the above assumption and condition, a 2D meso-scale model is established using ABAQUS, the representative volume element (RVE) with 0.025 mm × 0.025 mm is extracted (Fig. 2a) to study its mechanical behavior. The periodic boundary condition is adopted, and with one end is clamped and the other end is loaded with the displacement control. The active particles are generated and randomly distributed, the shape of which is simplified as a sphere, i.e. circular shape in the 2D model. The diameter of the particles ranges from 5 μm to 15 μm with the average size of 10 μm [36]. The particles present mono-model distribution, and specific size distribution of the particles is listed in Table 1 referring to the Ref [37] with the corresponding size scaled up. The pore between particle and binder is also built with the ellipse shape, the size distribution of which is followed by Ref. [33]. The modulus of the graphite is about 20–100 GPa [38,39], set as 50 GPa in the model, which is about four magnitudes larger than that of the binder [40] so that the particle can be regarded as a rigid body during modeling. The Young's modulus and yield stress of the active material can be obtained through the meso-scale model by inputting the mechanical behavior of the particle (already known) and the binder (setting initial assumptive values). The mechanical behaviors of binder can be finally determined through multiple iterations until the

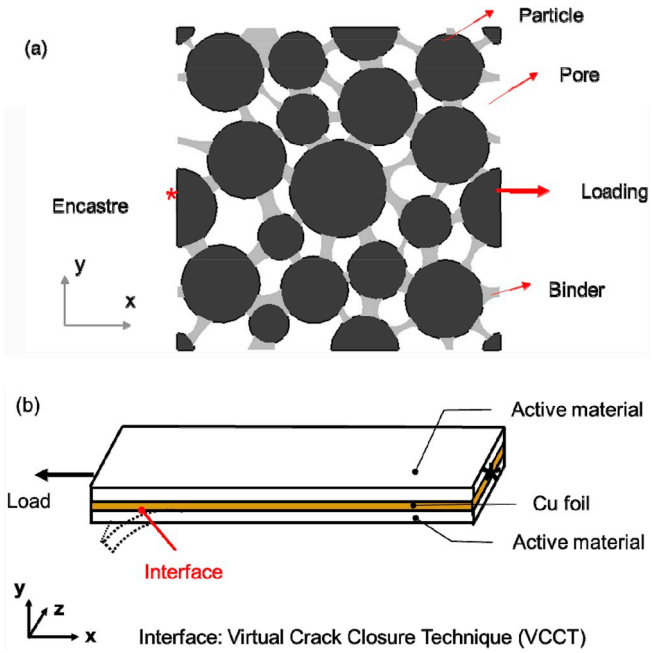

Fig. 2. Schematic illustration of (a) active material meso-scale modeling where active particles are randomly distributed within the binder. One end is fixed while another end is set for loading; (b) anode material modeling with three layers structure, where the interface between the active material and copper foil is modeled by virtual crack closure technique. One end is fixed while another end is set for loading.

Table 1
Particle size distribution of RVE model.

Particle diameter (μm)	Particle number in RVE
5	1
6	1
7	1
8	2
9	2
10.36	3
12	7
15	1

output mechanical behaviors of active material have the same values with the analytical values mentioned in Section 2.1.

2.3. Anode material modeling

Three-layer model is established based on the actual structure of the anode with one end clamped and the other end loaded as shown in Fig. 2b. The interface between the active material and copper foil is modeled by the virtual crack closure technique (VCCT) because the interface debonding often occurs during a tensile test. VCCT uses the principle of linear elastic fracture mechanics which can be used for problems with delamination growth along predefined surfaces. Crack propagation analysis is carried out on a nodal basis, i.e. the crack-tip node debonds when the fracture criterion, f, reaches the value 1. The fracture criterion is defined as follows:

$$f = \frac{G_{equiv}}{G_{equivC}} \geq 1 \tag{1}$$

where G_{equiv} is the equivalent strain energy release rate calculated at a node, and G_{equivC} is the critical equivalent strain energy release rate calculated based on the following formula

$$G_{equivC} = G_{IC} + (G_{IIC} - G_{IC})\left(\frac{G_{II} + G_{III}}{G_I + G_{II} + G_{III}}\right)^{\eta} \tag{2}$$

The critical fracture energy release rates G_{IC}, G_{IIC}, G_{IIIC} in Mode I, Mode II and Mode III are the options of the virtual crack closure technique, which determine the failure of the interface. The interfacial crack propagation here along one direction, mainly effected by the G_{IC}. Besides, simulations with different values of G_{IIC}, G_{IIIC} and η have been compared and proved to have little influence on interfacial adhesive strength (the maximum stress between copper foil and the active material layer). Therefore, we set the $G_{IIC} = G_{IIIC} = 0.5G_{IC} = 4.8 \times 10^{-6}$ N/mm, $\eta = 1.75$. As such, the parameters set here are validated by the peel-off simulation, with the interfacial adhesive strength estimated as 270 kPa [41]. The effect of interfacial adhesive strength will be further discussed in Section 4.2.

Drucker-Prager model is often used to model frictional materials, such as granular-like soils and rock. Considering the similarity in its mechanics nature, it is chosen to describe the mechanical behavior of the active material in this paper. The evolution of the yield surface with plastic deformation is described in terms of the equivalent stress $\overline{\sigma}$, which is chosen as the uniaxial tension yield stress, expressed as $\overline{\sigma} = \sigma_t(\overline{\varepsilon}^{pl}, \dot{\overline{\varepsilon}}^{pl})$, where $\dot{\overline{\varepsilon}}^{pl}$ is the equivalent plastic strain-rate, $\overline{\varepsilon}^{pl} = \int_0^t \dot{\overline{\varepsilon}}^{pl} dt$ is the equivalent plastic strain. Refer to the Ref. [42], linear yield criterion is adopted for anode, the angle of friction β equals to dilation angle ψ, which are both set as 70.9°, the flow stress ratio K is set as the default value 1. The critical mechanical properties of the active material are listed in Table 2, in which the elastic-plastic behaviors are obtained from the analytical calculation, and the failure properties are determined through simulation (anode material model) compared with the experimental results. The damage initiation in the Table 2 refers to the initiation strain of the damage. The damage evolution is used to describe the post-damage initiation behavior, assumes that damage is characterized by the progressive degradation of the material stiffness, leading to material failure. The damage evolution $\overline{u}_f^{pl}$ means the material stiffness will be fully degraded when the effective plastic displacement $\overline{u}^{pl}$ reaches the value $\overline{u}^{pl} = \overline{u}_f^{pl}$.

The metallic material model is used to describe the copper foil. The main mechanical properties at various strain-rates are summarized in Table 3 which have been validated by simulations shown in Fig. 3. Note that the failure strain of the copper foil obtained from the tensile test is a bit smaller than the actual failure strain of the copper foil without soaking in methanol and ultrasonic which calibrated by the anode simulation. This is because the fabrication of the copper foil sample through soaking in methanol and cleaning by an ultrasound cleaner will cause the earlier failure of the copper foil [29]. The failure of the copper foil is recalculated for better calibration, which is also summarized in Table 3 via anode material simulation calibration. The ductile criterion is adopted to describe its failure properties, i.e. the equivalent plastic strain at the onset of damage $\overline{\varepsilon}_D^{pl}$ is set as plastic failure strain. Solid elements are used to represent both active layer and copper foil layer in a total of 2750 elements.

Table 2
Mechanical properties of active material under different strain-rates through analytical calculation and simulation (anode material model).

Strain-rate/s^{-1}	Modulus/MPa	Drucker Prager Hardening/MPa	Damage Initiation	Damage Evolution $\overline{u}_f^{pl}$
5×10^{-4}	2000	2.7	0.048	0.003
5×10^{-3}		3.4	0.032	0.004
1×10^{-1}		6.8	0.0008	0.011

Table 3
Summarization of mechanical properties of copper foil at various strain-rates.

Strain-rate (s^{-1})	Modulus (GPa)	Yield stress (MPa)	Plastic failure strain $\bar{\varepsilon}_D^{pl}$	
			Experiment	Simulation calibration
5×10^{-4}	28	70	0.04	0.052
5×10^{-3}		75.6	0.038	0.051
1×10^{-1}		94.9	0.03	0.050

3. Results

3.1. Active material

As a mixed material, active material expresses obvious strain-rate dependency illustrated in Figs. 4a–c. Results show that meso-scale simulation results agree well with analytical calculation in elastic and plastic stage, especially the effective modulus and the yield stress. Therefore, the meso-scale model of active material is validated. The yield stress increases with the strain-rate, which shows the strain-rate hardening phenomena. The morphologies of stress concentration at different strain-rates all show the '~' type. There is a long plastic region of active material at the strain-rate of 5×10^{-4}/s and 5×10^{-3}/s, however, the failure occurs once the active material yields at the strain-rate of 0.1/s. It can be inferred that the failure of the active material is also strain-rate dependent. Besides, it can be observed that the stress concentration occurred along the binder area which means the failure of the active material is caused by the failure of binder. Analogies to other binder-particle materials, Yonezu et al. [43] also observed the micro-cracks of binder through the acoustic emission (AE) technique, and found that fracture of the porous silicon carbide was caused by the microcracks of binder, which was also loading rate dependent.

3.2. Anode material

With the proper establishment of constitutive models of binder, active particles and current collector, we may further assemble all component materials into anode and the constitutive deformation behavior of anode material can be obtained and illustrated in Fig. 5a. Good agreement can be found between computational results and experiments. The failure strain of the active material differ greatly under different strain-rates, showing the change of the mechanical behavior of anode from elastic-plastic behavior to elastic-brittle behavior.

Failure mechanism and morphology are analyzed based on the anode material simulation shown in Figs. 5b–c. Under relatively low strain-rate, e.g. 5×10^{-4}/s (Fig. 5b), the failure of the anode can be divided into three stages: Stage I: the debonding between active layer and copper layer happens after the material enters yield stage; Stage II: the active material fails followed by the drop of force; and Stage III: the copper layer fails with the further drop of force. The yield strain ε_{y1} of the active material is 0.0013 which is smaller than ε_{y2} of copper foil, where $\varepsilon_y = \sigma_y/E$. As a three-layer structure, the non-uniform deformation of three layers occurs when the tensile strain reaches ε_{y1}, then shear stress τ_{12} occurs and debonding happens when the shear stress is larger than the interfacial strength between two layers. Here, three layers show the different tensile displacements (U_x) in loading direction in stage I, leading to the occurrence of the interface slips (i.e. deboning). Besides, the interfacial strength between binder and copper layer is smaller than both adhesive strength of binder and the interfacial strength between binder and particle (e.g. strength of active material) [22], and thus, the debonding between binder and copper layer occurs firstly. This phenomenon can also be found in experiments where deboning occurs between the active layer and copper foil through observing the failure morphology as illustrated in the previous study [29]. The failures of the two materials are determined by their respective plastic failure strains.

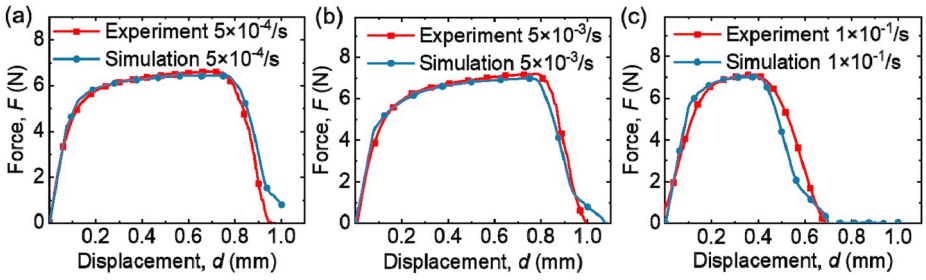

Fig. 3. Mechanical properties validation through simulation compared with experiments [29] of copper at various strain-rates: (a) 5×10^{-4}/s; (b) 5×10^{-3}/s; (c) 1×10^{-1}/s.

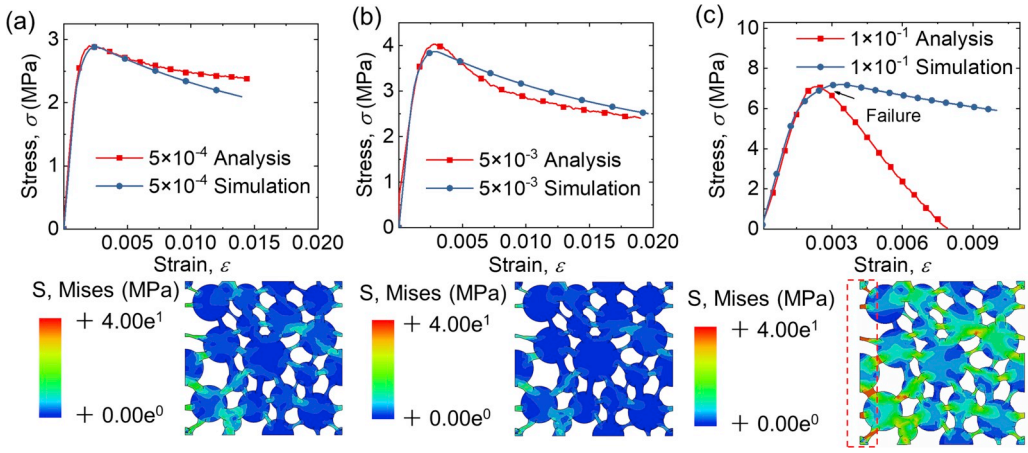

Fig. 4. Comparison of analytical and simulated stress-strain curves for active material at different strain-rates: (a) 5×10^{-4}/s; (b) 5×10^{-3}/s; (c) 1×10^{-1}/s.

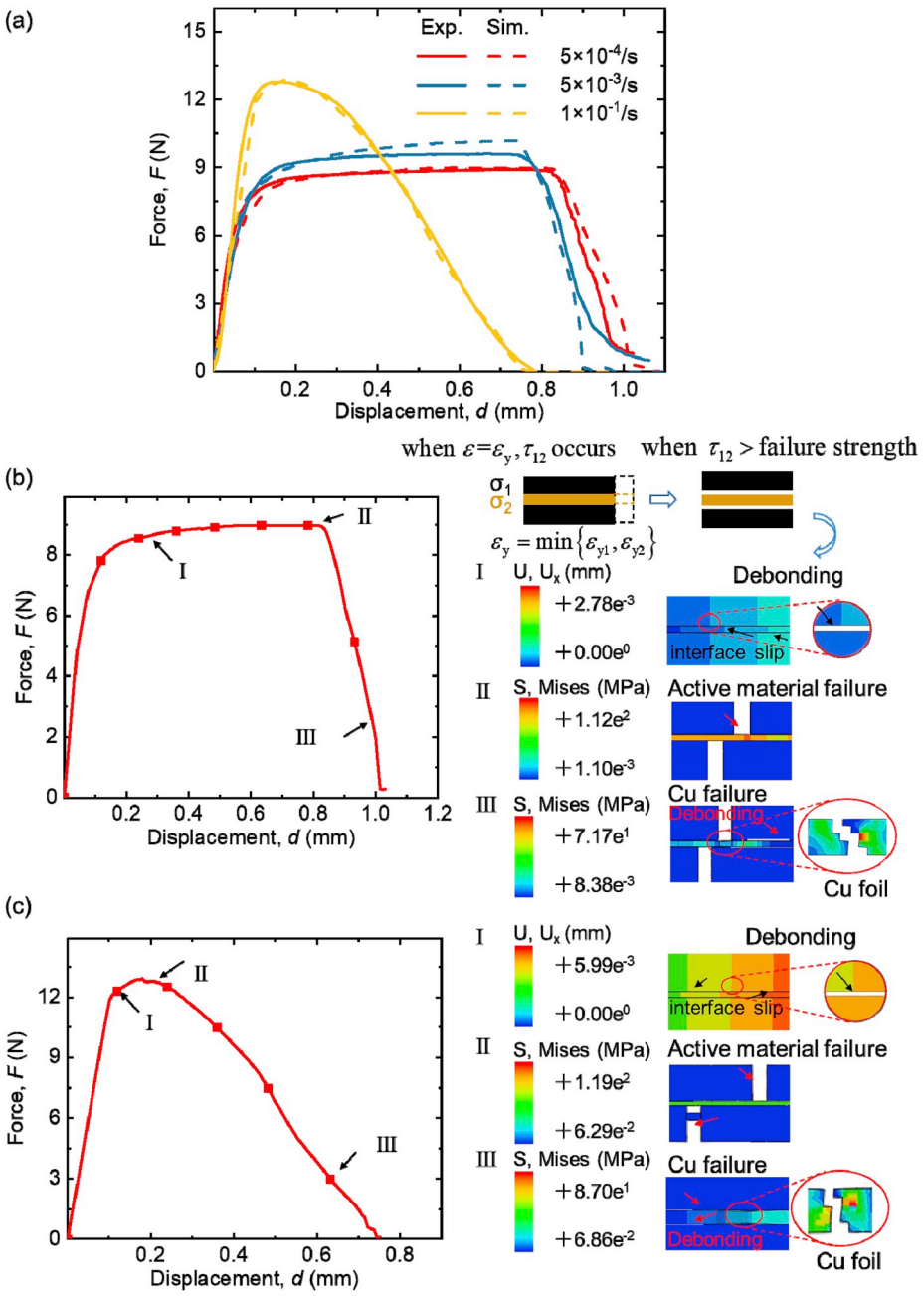

Fig. 5. (a) Comparison of experimental [29] and simulated force-displacement curves for anode material at strain-rates of 5×10^{-4}/s, 5×10^{-3}/s, and 1×10^{-1}/s; Failure mechanism and morphology of anode in tensile tests at different strain-rates: (b) 5×10^{-4}/s; (c) 1×10^{-1}/s.

Active material reaches its plastic failure strain earlier than copper foil with the failure points of both active material and copper foil are noted in Figs. 5b–c. Therefore, some cracks on the surface of anode can be observed in experiments [29]. The failure of the active material is much earlier at high strain-rate than low strain-rate, which is probably one of the major reasons causing the earlier short-circuit of the battery.

4. Discussion

4.1. Particle size distribution and mechanical properties effect

Natural microcrystalline graphite with narrow particle size distribution and high sphericity exhibits excellent electrochemical performance [36]. Therefore, it is interesting to investigate how the particle size distribution influence the mechanical integrity of the active material. Here, particles with uniform distribution and mono-model distribution were discussed to investigate mechanical behaviors of the active material shown in Fig. 6. 18 particles with the same size of 10 μm are built in uniform distribution model. The volume fraction of pore, binder and particles are the same as mono-model distribution mentioned before. Results show that the modulus of active material in both two distribution models were almost same which means the particle size distribution has little influence on modulus. Deformation morphology with stress state distribution in two typical moments were extracted. Results show part of binder yields in mono-model in t_1 with black circle noted, causing the earlier yield of the active material. Both two different particle distributions have the identical maximum stress. After reaching the maximum stress, the stress starts to decrease, the decrease rate in mono-model distribution is larger than that in uniform distribution. The stress state distribution in t_2 shows most of the binder yields in

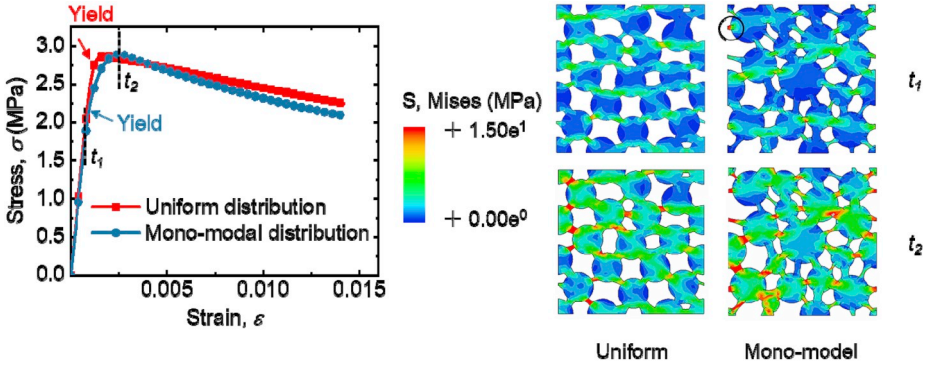

Fig. 6. Stress-strain curves of active material with different particle size distribution.

mono-model distribution, casing the large rate decrease of stress. To sum up, active material with uniform particle size distribution have a better mechanical performance than that with mono-model distribution. Therefore, it is important to control the uniformity of particle size distribution in terms of both electrochemical and mechanical aspects.

The mechanical behavior of binder cannot be directly obtained from experiments so the critical parameters of the binder are obtained based on the meso-scale simulation (Table 4). The modulus of binder with different strain rates ranges from 2.5 GPa to 5 GPa, and the yield stress ranges from 14.5 MPa to 36.5 MPa, which is on the same order of magnitude as the experimental results of CMC [44]. Binder shows an obvious strain-rate tendency, the effective modulus and the yield stress increase with the strain-rate. As a viscoelastic material, the increases of Young's modulus and yield stress with strain-rate have been commonly observed. Mulliken et al. [45] discovered that binder material exhibited increased strain-rate sensitivity of yield stress as the beta-transition of the viscoelastic behavior. Though binder's effective modulus is strain-rate dependent, the modulus of active material does not show obvious strain-rate dependency for the relatively lower binder proportion and lower modulus compared with graphite particles. However, the strain rate of yield stress on the anode show the same trend with that on binder.

4.2. Interfacial strength effect

Previous study discovered that the interfacial adhesive strength σ_s between the copper foil and active layer is affected by the binder contents, which decreases with increasing binder content [22]. Therefore, the effect of interfacial adhesive strength varying from 9.6 kPa to 6.4 MPa is discussed at different strain-rates shown in Figs. 7a–c. The failure strain of the anode decreases firstly then increases with the adhesive strength σ_s, the critical adhesive strength σ_{crs} is about 1 MPa. Critical adhesive strength is defined as the strength threshold when the debonding occurs. When $\sigma_s < \sigma_{crs}$, the interfacial slip occurs before material failure. Each layer of the anode will deform freely if the $\sigma_s = 0$, the failure of the materials would not affect each other. The increase of σ_s needs more plastic work to overcome interface viscosity, the failure of the materials affects each other, eventually causing the earlier failure. However, no interfacial slip occurs when $\sigma_s > \sigma_{crs}$, the interfacial viscosity coordinates deformation of the three layers. The increase of σ_s increases its interface compatibility, finally leading to the larger failure strain. The failure morphologies change from oblique fracture surface to flat fracture surface (Fig. 7d). This also evidences that the interfacial slip is obvious in low adhesive strength, and there is no interfacial slip observed in high adhesive strength.

Table 4
Mechanical properties of binder obtained based on meso-scale simulation.

Strain-rate/s^{-1}	Modulus/MPa	Yield stress/MPa
5×10^{-4}	2500	14.5
5×10^{-3}	3000	19.5
1×10^{-1}	5000	36.5

4.3. Thickness effect

The thickness of the active layer is essential for the determination of electrical properties, e.g. capacity, and energy density. In the meantime, due to the sandwiched structure of anode material, the thicker active layer may have impacts on the overall mechanical integrity of the anode. Firstly, the thickness ratio between the active materials and current collectors defined as $\eta = t_1/t_2$. Then, the thickness ratio η various from 2 to 7.8 on mechanical behaviors of active material at different strain-rates are computed. The critical values, i.e. yield stress and modulus are summarized by the coupling effects of strain-rate and thickness ratio (Figs. 8a–b). The yield stress decreases with the thickness ratio at all strain-rates (Fig. 8a). The modulus decreases with the thickness ratio and has little effect by strain-rate (Fig. 8b). Therefore, it is recommended to have a low thickness for good mechanical integrity of anode.

5. Conclusions

Anode plays an important role in the internal short-circuit and thermal runaway behaviors of lithium-ion batteries. However, the fundamental mechanisms of mechanical behaviors of anode material upon various strain-rates remain unknown. In this paper, a three-layer detailed anode model is established with the consideration of strain-rate. The mechanical properties of the copper foil and active material are obtained from the experiments and analytical calculation, respectively, both validated by the simulation. Results show that the model is capable to accurately describe and predict the mechanical behavior for the anode. With the help of the established computational model, it is discovered that debonding between the active material and copper foil occurs initially during tensile loading followed by the failure of the two materials. The earlier failure of the active material under high strain-rate is probably one of the dominant causes of the earlier short-circuit of the battery under dynamic impact. In the meantime, results show that active material with uniform particle size distribution shows good performance in mechanical properties, and the mechanical properties increase with the thickness ratio of active material and current collector. The model developed here unravels the mechanism of the strain-rate dependency of the anode. Further, it is found that the failure of the anode is affected by the interfacial adhesive strength. The failure strain decreases and then increases with the adhesive strength.

Results shed light on the comprehensive understanding of the strain-rate effect of the anode, and guide the safety design of lithium-ion batteries as well as their evaluation, and monitoring during service. The limitation of this study is that the 2D meso-scale model is not able to predict crack nucleation and propagation within active material which would be equally beneficial for understanding possible failure of anode

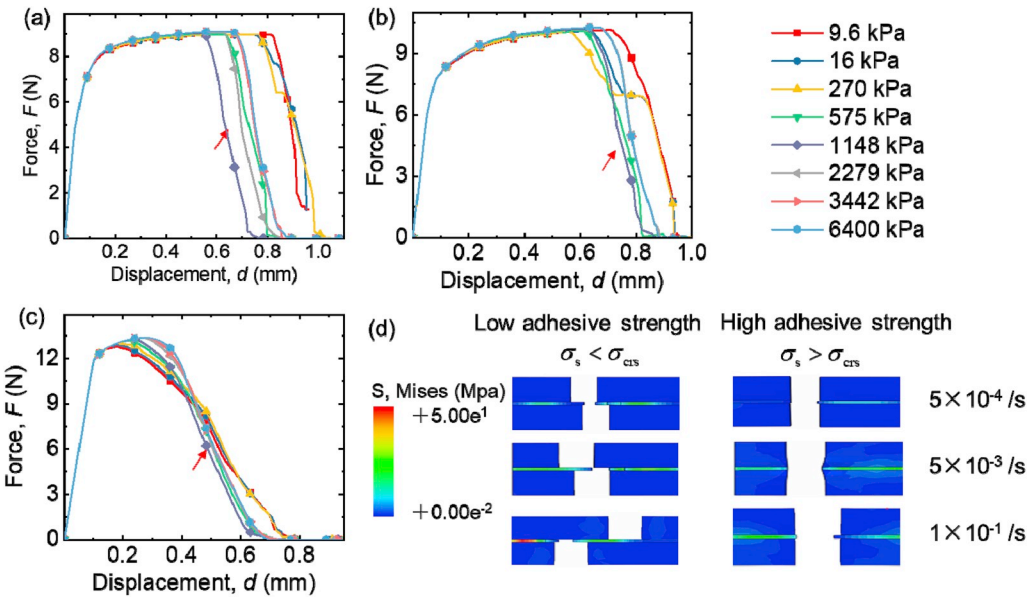

Fig. 7. Force-displacement curves of anode with various interfacial adhesive strength from 9.6 kPa to 6400 kPa at different strain-rate: (a) 5×10^{-4}/s; (b) 5×10^{-3}/s;
(c) 1×10^{-1}/s; (d) Comparison of the failure morphology with different interfacial adhesive strength at various strain-rate of 5×10^{-4}/s, 5×10^{-3}/s, and 1×10^{-1}/s.

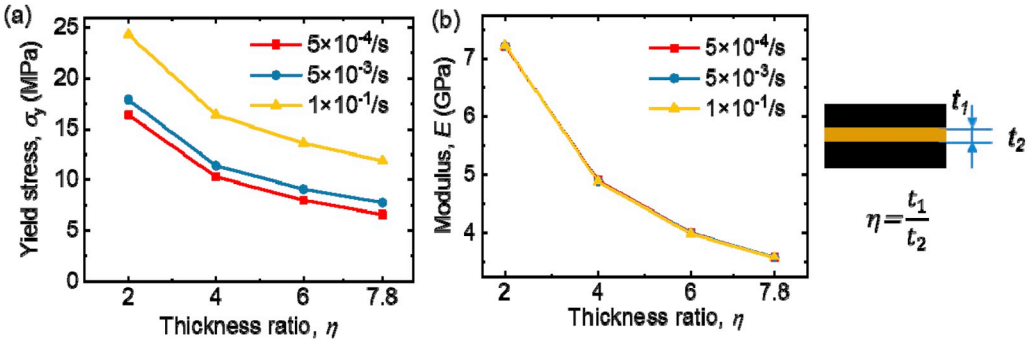

Fig. 8. The stress-strain curves of anode material with different thickness ratio at strain-rate of (a) 5×10^{-4}/s; (b) 5×10^{-3}/s; (c) 1×10^{-1}/s; The critical parameters of anode material with thickness ratio: (d) yield stress and (e) modulus.

and it will be investigated in the future study.

Author contribution

J.X. conceived the study. L.W., X.D., B.L. conducted the experiment and established FE model. X.D., B.L, S.Y., Q.L. and J.X. analyzed the data. L.W. and J.X. wrote the manuscript.

Declaration of competing interest

The authors declare that they have no known competing financial interests or personal relationships that could have appeared to influence the work reported in this paper.

Acknowledgments

This work is financially supported by The National Science Foundation of China (11872099 and 11902022), The National Key Research and Development Program of China (2017YFB0103703), China Postdoctoral Science Foundation (2019M650439 and 2019TQ0017), Opening Fund of Key Laboratory of Impact and Safety Engineering (Ningbo University), Ministry of Education (cj201907).

Appendix A. Supplementary data

Supplementary data to this article can be found online at https://doi.org/10.1016/j.jpowsour.2019.227468.

References

[1] J.B. Goodenough, Y. Kim, Chem. Mater. 22 (2010) 587–603.
[2] J. Xu, Y. Jia, B. Liu, H. Zhao, H. Yu, J. Li, S. Yin, Exp. Mech. 58 (2018) 633–643.
[3] B.H. Liu, Y.K. Jia, J. Li, S. Yin, C.H. Yuan, Z.H. Hu, L.B. Wang, Y.X. Li, J. Xu, J. Mater. Chem. A 6 (2018) 21475–21484.
[4] D.P. Finegan, E. Darcy, M. Keyser, B. Tjaden, T.M.M. Heenan, R. Jervis, J.J. Bailey, R. Malik, N.T. Vo, O.V. Magdysyuk, R. Atwood, M. Drakopoulos, M. DiMichiel, A. Rack, G. Hinds, D.J.L. Brett, P.R. Shearing, Energy Environ. Sci. 10 (2017) 1377–1388.
[5] M.R. Palacin, A. de Guibert, Science 351 (2016) 7.
[6] Q. Wang, P. Ping, X. Zhao, G. Chu, J. Sun, C. Chen, J. Power Sources 208 (2012) 210–224.
[7] N. Iqbal, S. Lee, J. Electrochem. Soc. 165 (2018) A1961–A1970.
[8] Y.Q. Sun, Q.O. Wu, G.Q. Shi, Energy Environ. Sci. 4 (2011) 1113–1132.
[9] B. Liu, H. Zhao, H. Yu, J. Li, J. Xu, Electrochim. Acta 256 (2017) 172–184.
[10] C. Lin, A.H. Tang, N.N. Wu, J.L. Xing, Nanomater. Nanotechnol. 6 (2016).
[11] A. Samba, N. Omar, H. Gualous, O. Capron, P. Van den Bossche, J. Van Mierlo, Electrochim. Acta 147 (2014) 319–329.
[12] Y. Jia, S. Yin, B. Liu, H. Zhao, H. Yu, J. Li, J. Xu, Energy 166 (2019) 951–960.
[13] B. Liu, S. Yin, J. Xu, Appl. Energy 183 (2016) 278–289.
[14] B. Liu, Y. Jia, C. Yuan, L. Wang, X. Gao, S. Yin, J. Xu, Energy Storage Mater. (2019). In Press.

[15] J. Xu, B. Liu, L. Wang, S. Shang, Eng. Fail. Anal. 53 (2015) 97–110.
[16] L.B. Wang, S. Yin, J. Xu, J. Power Sources 413 (2019) 284–292.
[17] H.X. Chen, Y. Xiao, L. Wang, Y. Yang, J. Power Sources 196 (2011) 6657–6662.
[18] Y.P. Wu, E. Rahm, R. Holze, J. Power Sources 114 (2003) 228–236.
[19] B. Liu, X. Wang, H.S. Chen, S. Chen, H. Yang, J. Xu, H. Jiang, D.N. Fang, J. Appl. Mech. Trans. ASME (2019) 86.
[20] Y.X. Ye, Y.Y. Feng, Z.C. Lian, Y.Q. Hua, Appl. Surf. Sci. 309 (2014) 240–249.
[21] C. Zhang, J. Xu, L. Cao, Z.N. Wu, S. Santhanagopalan, J. Power Sources 357 (2017) 126–137.
[22] J.C. Chen, J.Y. Liu, Y. Qi, T. Sun, X.D. Li, J. Electrochem. Soc. 160 (2013) A1502–A1509.
[23] K.J. Chung, C.F. Lin, W.C. Chiang, Trans. Can. Soc. Mech. Eng. 37 (2013) 861–871.
[24] S.W. Kim, X.Y. Li, H.J. Gao, S. Kumar, Acta Mater. 60 (2012) 2959–2972.
[25] S. Choi, T.W. Kwon, A. Coskun, J.W. Choi, Science 357 (2017) 279–283.
[26] H.C. Chu, H.Y. Tuan, J. Power Sources 346 (2017) 40–48.
[27] C.X. Huang, K. Wang, S.D. Wu, Z.F. Zhang, G.Y. Li, S.X. Li, Acta Mater. 54 (2006) 655–665.
[28] T. Yim, S.J. Choi, Y.N. Jo, T.-H. Kim, K.J. Kim, G. Jeong, Y.-J. Kim, Electrochim. Acta 136 (2014) 112–120.
[29] L.B. Wang, S. Yin, C. Zhang, Y. Huan, J. Xu, J. Power Sources 392 (2018) 265–273.
[30] M. Dao, L. Lu, Y.F. Shen, S. Suresh, Acta Mater. 54 (2006) 5421–5432.
[31] Z. Lu, M. Lugo, M.H. Santare, A.M. Karlsson, F.C. Busby, P. Walsh, J. Power Sources 214 (2012) 130–136.
[32] A.W. Golubkov, S. Scheikl, R. Planteu, G. Voitic, H. Wiltsche, C. Stangl, G. Fauler, A. Thaler, V. Hacker, RSC Adv. 5 (2015) 57171–57186.
[33] S. He, J. Zeng, B.T. Habte, F. Jiang, Sci. Bull. 61 (2016) 656–664.
[34] C. Meyer, H. Bockholt, W. Haselrieder, A. Kwade, J. Mater. Process. Technol. 249 (2017) 172–178.
[35] E.K. Rahani, V.B. Shenoy, J. Electrochem. Soc. 160 (2013) A1153–A1162.
[36] C. Wang, G. Gai, Y. Yang, JOM (J. Occup. Med.) 70 (2018) 1392–1397.
[37] Q. Liu, T. Zhang, C. Bindra, J.E. Fischer, J.Y. Josefowicz, J. Power Sources 68 (1997) 287–290.
[38] Y. Qi, H.B. Guo, L.G. Hector, A. Timmons, J. Electrochem. Soc. 157 (2010) A558–A566.
[39] X. Gao, P. He, J. Ren, J. Xu, Energy Storage Mater. 18 (2019) 23–33.
[40] R. Kuruba, M.K. Datta, K. Damodaran, P.H. Jampani, B. Gattu, P.P. Patel, P. M. Shanthi, S. Damle, P.N. Kumta, J. Power Sources 298 (2015) 331–340.
[41] C.Y. Dai, Z. Wang, K. Liu, X.X. Zhu, X.B. Liao, X. Chen, Y. Pan, Eng. Fail. Anal. 101 (2019) 193–205.
[42] J.E. Zhu, W. Li, Y. Xia, E. Sahraei, J. Electrochem. Soc. 165 (2018) A1160–A1168.
[43] A. Yonezu, X. Chen, Ceram. Int. 40 (2014) 9859–9866.
[44] Y. Wang, D. Dang, D. Li, J. Hu, Y.-T. Cheng, J. Power Sources 425 (2019) 170–178.
[45] A.D. Mulliken, M.C. Boyce, Int. J. Solids Struct. 43 (2006) 1331–1356.